Rapid Fabrication of Antimony-Impregnated Graphite Composites via Spark Plasma Sintering

A. Sedaghat Ahangari Hossein Zadeh*, M. R. Rahimipour, M. Shirani

Department of Ceramic, Materials and Energy Research Centre, Karaj, Iran.
Received: 15 December 2024 - Accepted: 22 April 2025

Abstract

In this study, a novel process for fabricating carbon composites saturated with molten metals was introduced and investigated. Using a spark plasma sintering (SPS) device, molten antimony was successfully impregnated into a cylindrical graphite sample. Mechanical pressure within the mold and suction caused by vacuum facilitated the rapid impregnation of antimony into the graphite pores. The results showed that the density, porosity percentage, and bending strength of the graphite before impregnation were 1.68 g/cm³, 21.1%, and 21 MPa, respectively. After impregnation with antimony, these values improved to 2.12 g/cm³, 14%, and 33 MPa. A notable observation was the complete filling of fine pores in the graphite, while some larger pores remained unfilled. This phenomenon can be attributed to the relationship between capillary force and pore diameter, where smaller pores are more easily filled due to higher capillary forces. In this project, the impregnation depth of antimony reached a remarkable 3 cm in just 9 minutes. Additionally, by analyzing punch displacement data, the precise timing of initial powder melting, impregnation into graphite pores, and process completion could be determined. The punch displacement halted at two stages: the first stop indicated complete powder sintering, and the second confirmed the completion of molten metal impregnation. The key advantages of this method are its high speed and significant impregnation depth.

Keywords: Graphite Composite, Antimony, Molten Metal Impregnation, Porosity, Capillary Action, SPS.

1. Introduction

The infiltration of molten metal into a preform to create composites is referred to as melt infiltration [1]. This process can be performed with or without external pressure. In melt infiltration, the reinforcing phase is first placed in a mold, and the molten alloy is infiltrated and then solidified. The process can be assisted by external forces such as mechanical pressure, gas pressure, vacuum, vapor, centrifugal force, etc. Fig. 1 illustrates methods of melt infiltration under gas pressure, mechanical pressure, and vacuum [2]. Carbon and graphite are inherently porous after molding and curing. To enhance strength, improve thermal conductivity, reduce resistance, decrease porosity, and achieve impermeability, they are saturated with various resins and metals. For example, saturating graphite with antimony can reduce porosity and minimize bubble formation, particularly in applications involving light hydrocarbons and hot oils. Some users report that saturants like babbitt (especially lead-based babbitt), silver, and antimony improve the frictional and wear characteristics of carbon/graphite and graphite. However, ST. MARYS CARBON has not observed this effect in laboratory tests. Antimony effectively reduces the porosity of carbon/graphite and graphite, partly due to its low surface tension. Table 1 shows the surface tension of molten metals used for saturating carbon and graphite at saturation temperatures.

*Corresponding author
Email address: a.sedaghat@merc.ac.ir

Antimony has a low melting point (630°C), which limits its application temperature [3].

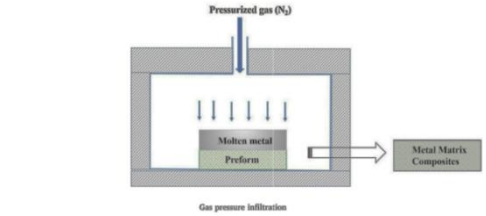

Fig. 1. Some methods of melt penetration [2].

Table. 1. Surface tension of molten carbon and graphite impregnating metals at impregnation temperature [3].

Metal	Surface Tension[1](mN/m)
Antimony (Sb)	367
Copper (Cu)	1290
Silver (Ag)	951
Tin (Sn)	570

1 at Impregnation Temperature

Resin-impregnated graphite is widely used in chlor-alkali, sulfuric acid, and petrochemical industries. Graphite alone exhibits excellent thermal stability, thermal conductivity, and corrosion resistance. Phenolic resin, used as a filler for graphite pores,

typically has high density but low operating temperatures, with a thermal expansion coefficient ten times that of graphite. Phenolic resin-impregnated graphite is often used in highly corrosive environments, such as acidic conditions [4].

Stec et al. [5] infiltrated molten iron into microporous carbon refractories using a furnace under 3 bar gas pressure, with a molybdenum disilicide heating element at 1500°C for 90 minutes. Ma et al. [6] fabricated carbon/aluminum composites with a compressive strength of 304 MPa using mechanical pressure infiltration. A pressure of 3 MPa and a temperature of 850°C were applied for 1 hour. Fig. 2 shows the process and resulting microstructure. The high strength was attributed to the formation of aluminum carbide at the interface.

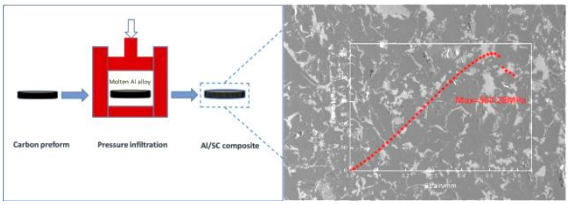

Fig. 2. The process of infiltrating molten aluminum into a carbon body and the resulting microstructure [6].

Li et al. [7] produced porous carbon bodies by hot pressing a mixture of petroleum coke, graphite, and carbon black at 150°C, followed by carbonization at 1150°C. Molten copper was then infiltrated into the porous carbon under mechanical pressure. Fig. 3 shows the microstructure of the resulting composite. The initial carbon body had a density of 1.66 g/cm³, while the composite achieved 2.52 g/cm³ and a bending strength of 47.52 MPa.

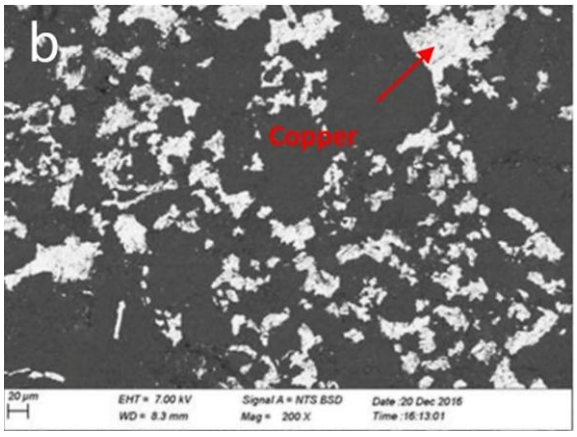

Fig. 3. Microstructure of carbon/copper composite fabricated by melt penetration under mechanical stress [7].

The aim of this study was to introduce a novel method for impregnating molten antimony into a graphite body and to examine the microstructure and mechanical properties of the resulting composite. The combination of mechanical pressure inside the mold and vacuum suction in the SPS chamber appears to significantly enhance molten metal infiltration into dense graphite. This study explores the feasibility of this process for impregnating porous bodies.

2. Materials and Methods

The materials used included a carbon (graphite) block and antimony powder. The graphite block was prepared under internal project No. 361391009 at the Materials and Energy Research Center. It was produced by milling primary carbon and graphite materials, followed by pressing and carbonization at 1050°C without pitch impregnation. The bulk density of the graphite block was 1.68 g/cm³, with an apparent porosity of 21.1%. Industrial-grade antimony powder (99% purity, 325 mesh) from China was used. Phase analysis was performed using an X-ray diffractometer (XRD, Philips PW 3710) with CuKα radiation (λ = 1.54 Å). The phases were identified using HighScore Xpert software. Microstructural analysis was conducted using a TESCAN VEGAII scanning electron microscope (SEM) equipped with an EDS spectrometer (Rontec). Optical microscopy images were analyzed using ImageJ software. Bending strength was measured using a SANTAM 20T testing machine, with sample dimensions of 6 × 4.5 mm, a span of 30 mm, and a loading rate of 0.21 mm/s.

The SPS device (EasyFashion Metal Products Co., China) had a maximum power of 100 kW and a compressive force of 20 tons. Temperature was measured using a thermocouple on the sample surface. To non-destructively assess the extent and geometry of antimony infiltration in the graphite matrix (Fig. 4), radiographic testing was conducted using Pars Precision Casting Company's equipment. The impregnated samples were sectioned longitudinally and subjected to X-ray examination from three orthogonal directions. The tests employed conventional radiography films with X-ray/gamma ray systems, ensuring complete coverage of the sample geometry regardless of its thickness or complexity. The radiographic technique operates on the principle of differential radiation absorption within the material. When radiation passes through the sample and interacts with the underlying film, variations in absorption caused by internal features (such as pores, inclusions, or cracks) create distinct contrast patterns on the developed film. This enables comprehensive detection and characterization of potential defects throughout the sample volume.

The process involved:

a. Placing 51.5 g antimony powder in a graphite mold (Fig.4) lined with three graphite foil layers (1 mm thick).

b. Applying minimal pressure (0.5 tons, 10 MPa) and current (0.04 A/min).

c. Monitoring temperature/displacement to determine melting (380°C surface, ~630°C center) and impregnation (9 minutes).
d. Sectioning the sample for density, microstructure, and strength analysis.

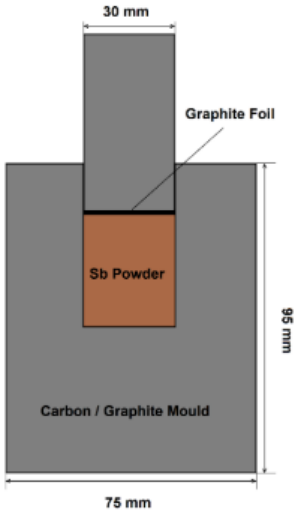

Fig. 4. Components and dimensions of the mold used in antimony infiltration using the SPS method.

3. Results and Discussion

3.1. X-ray Imaging of Impregnated Samples

Fig. 5. displays X-ray images of the samples from a top-view perspective. Radiographic testing employs gamma and X-rays, which possess high penetration capabilities through various materials, enabling material examination and defect detection in products. In this method, X-ray or radioactive beams are directed at the sample, and after passing through, they are reflected onto a film. Variations in internal thickness and structural characteristics cause certain areas to appear darker or lighter on the film.

X-rays and gamma rays have extremely short wavelengths, endowing them with high energy and significant penetration power. As these beams traverse any medium, they undergo attenuation and partial absorption. The degree of attenuation depends on several factors, including the density and structure of the medium, as well as the type, intensity, and energy of the radiation. The fundamental principle of this method lies in the variation of absorption coefficients and the differential transmission of radiation through sound versus defective regions of the sample. Any defect with a density differing from that of the base material will alter the radiation transmission, either increasing or decreasing it.

Defects such as oxide particles, which have a higher density than the sample, exhibit greater absorption coefficients, reducing the intensity of transmitted radiation and appearing lighter on the film. Conversely, defects like pores or gas pockets, with lower density, appear darker due to reduced absorption. Precise interpretation of the film, combined with knowledge of the sample's processing history, allows for accurate identification of internal defects or anomalies. Radiation absorption is directly proportional to the mass of the material, which depends on its density, chemical composition, and thickness. Generally, materials with higher atomic numbers absorb more radiation, allowing less to reach the film, while thinner sections permit greater transmission.

Key Observations:

- Darker regions in the image indicate areas where radiation penetration was easier, resulting in more radiation reaching the film.
- Lighter regions signify greater absorption, making penetration more difficult.
- In the fabricated sample, which consists solely of carbon and antimony:
  - Black areas correspond to porous carbon (atomic mass: 12 g/mol; theoretical density: 2.2 g/cm³).
  - White areas represent antimony-filled pores (atomic mass: 121.7 g/mol; density: 6.7 g/cm³).

Fig. 5. reveals preferential infiltration patterns of antimony within the graphite structure, attributable to the anisotropic nature of the original graphite block produced via bidirectional pressing [12,13]. This manufacturing method induced preferential grain orientation and consequent non-uniform pore distribution, leading to heterogeneous melt penetration. The phenomenon is further exacerbated by non-uniform current distribution during spark plasma sintering, creating localized temperature gradients that reduce melt viscosity and promote directional flow toward higher-temperature regions [12]. Comparative analysis suggests that isostatic pressing could potentially yield more uniform, circular infiltration patterns. The observed hair-like penetration fronts provide clear evidence of capillary action-driven impregnation through graphite pores. Notably, the significant resistivity contrast between antimony (~4×10^{-7} Ω·m) and graphite (5-30×10^{-6} Ω·m) [12, 13] facilitates localized current concentration in antimony, accelerating its melting. Radiographic analysis confirms the effectiveness of graphite foil barriers, evidenced by distinct dark circular regions where molten antimony was successfully contained within the graphite cylinder. This containment is attributed to the foil's pore structure being incompatible with melt penetration toward the punch region.

Fig. 6. (side-view X-ray) highlights three key findings:
a. Greater downward infiltration due to increased melt availability and gravitational effects.
b. An ellipsoidal distribution pattern of antimony, resulting from graphite anisotropy.
c. A maximum infiltration depth of ~30 mm, achieved through combined mechanical pressure (punch) and vacuum suction.
The process terminated once the antimony supply was depleted. Theoretical deeper infiltration might be possible with an unlimited melt reservoir, though

practical design limitations currently prevent testing this hypothesis.

This analysis demonstrates how X-ray radiography provides critical insights into:

- Melt infiltration patterns
- Depth quantification
- Process efficiency
- The effects of structural anisotropy

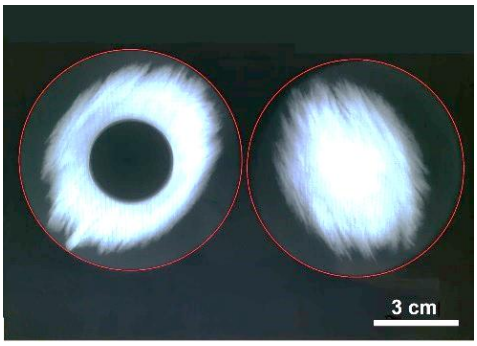

Fig. 5. X-ray image of infiltrated samples (top view).

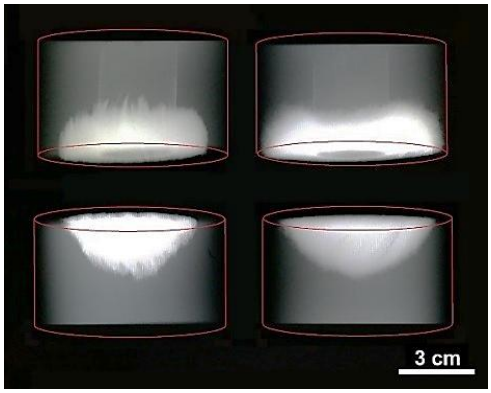

Fig. 6. X-ray image of infiltrated samples (side view).

3.2. Post-Process Analysis and Thermal Behavior During SPS Infiltration

Following punch extraction from the graphite mold, no residual antimony was observed in the cavity, confirming complete melt infiltration into the graphite matrix or potential leakage through punch-mold interfaces. While no visible melt leakage was detected, the presence of white deposits on the SPS chamber walls indicated antimony vaporization [12]. Mass balance calculations revealed that 51.5 g of antimony powder was primarily infiltrated into the graphite, with only 2.7 g lost through vaporization. The vapor escape likely occurred through interconnected porosity in the graphite and micro-gaps at the punch-mold interface. Fig. 7. presents the temperature-displacement profile during SPS processing.

The surface thermocouple recorded 250°C at complete sintering (Stage 1: 26 min), while the central region (antimony location) undoubtedly exceeded 630°C due to: (i) current concentration in lower-resistivity antimony (4×10^{-7} Ωm vs. graphite's 5-30$\times10^{-6}$ Ωm) [12,13], and (ii) significant thermal gradient across the mold. Stage 2 (9 min duration) commenced at 380°C surface temperature (~630°C center), featuring simultaneous antimony melting and infiltration into graphite pores.

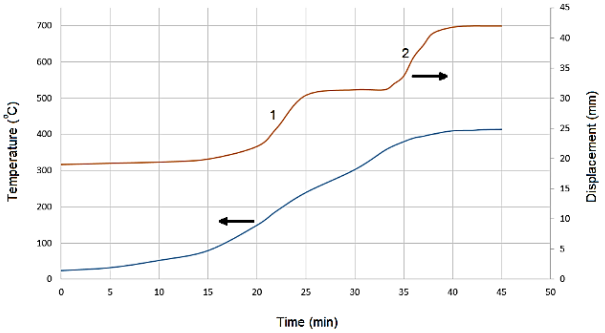

Fig. 7. Temperature and displacement versus time graph for the SPS process for antimony infiltration.

The punch displacement plateau at this stage confirmed complete impregnation, achieved through synergistic mechanical pressure (10 MPa) and vacuum-assisted capillary action. This two-stage process enabled full melt penetration within 9 minutes, with negligible interference from graphite's thermal expansion due to the powder column height.

3.3. Phase Composition and Microstructural Characterization

Fig. 8. presents the phase composition analysis of the graphite/antimony composite, revealing only distinct graphite and antimony phases without any detectable interfacial compounds.

The broadening of graphite's primary peaks suggests the presence of amorphous carbon within the composite. SEM analysis (Fig. 9 and Fig.10) at 100× and 400× magnification with elemental mapping confirms this phase separation, where white regions correspond to antimony (density: 6.7 g/cm³) and gray areas represent carbon (density: 2.2 g/cm³).

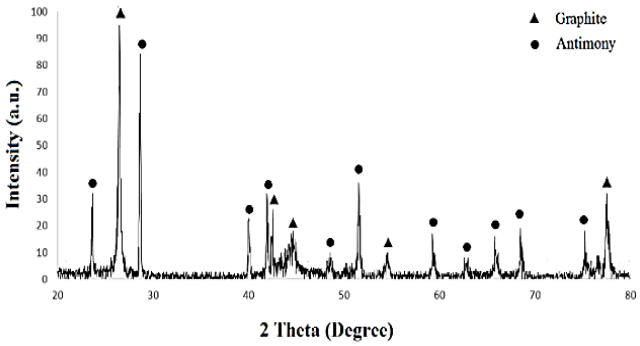

Fig. 8. X-ray diffraction pattern of graphite/antimony composite.

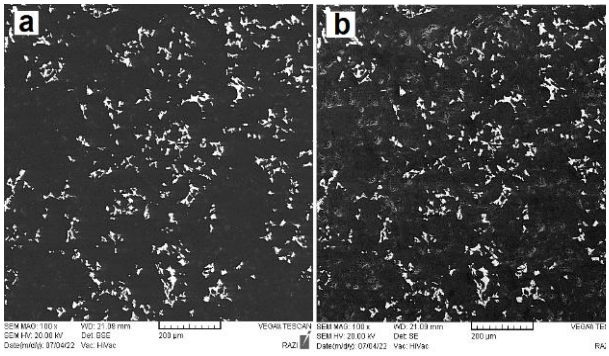

Fig, 9. SEM micrographs of graphite/antimony composite at 100× magnification: (a) backscattered electron mode (b) secondary electron mode.

Secondary electron imaging effectively demonstrated the surface morphology and pore filling efficiency, showing complete infiltration of most graphite pores by antimony, though some larger pores remained unfilled due to inaccessible melt pathways.
The directional infiltration pattern visible in low-magnification SEM (Fig. 11.) originates from the anisotropic pore structure of the axially pressed graphite preform.

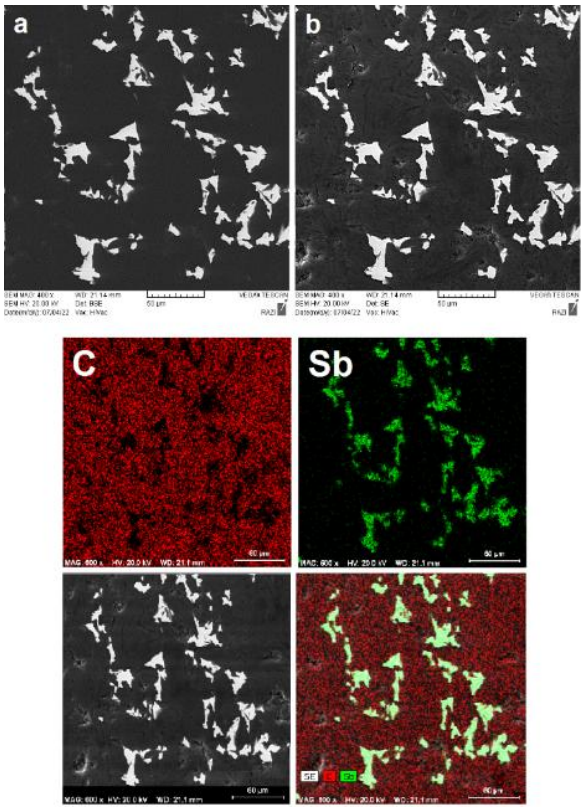

Fig. 10. SEM micrographs of graphite/antimony composite at 400× magnification (a: backscattered electron mode, b: secondary electron mode) with elemental map of carbon (C) and antimony (Sb).

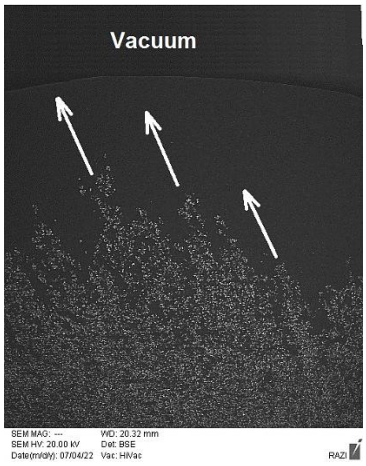

Fig. 11. SEM image at lowest magnification of the surface of graphite infiltrated with antimony.

The pristine graphite's porous structure (Fig. 12.), formed during pyrolysis and carbonization of precursor materials, exhibited 21.1% open porosity and 1.68 g/cm³ density via Archimedes testing. Optical micrographs at 50× and 200× magnification reveal the interconnected pore network responsible for the material's initial bending strength of 21 MPa. The pore morphology directly results from gaseous byproduct evolution during the carbonization process at 1050°C.

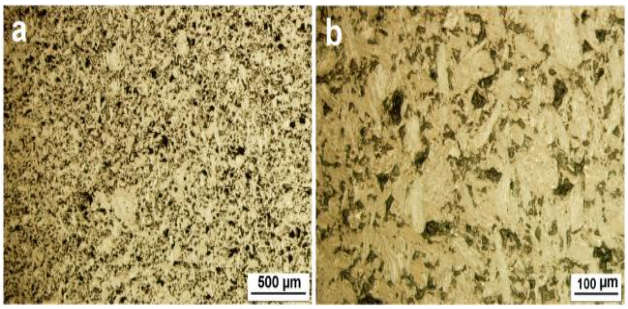

Fig. 12. Optical micrographs of graphite at (a) 50× and (b) 200× magnification.

Post-impregnation optical microscopy (Fig. 13) demonstrates selective pore filling, where antimony completely infiltrated fine pores (down to 1 µm diameter) while leaving larger voids unfilled.
This size-dependent infiltration behavior increased the composite's density to 2.12 g/cm³ and reduced porosity to 14%, concurrently enhancing bending strength to 33 MPa. The 1000× magnification images particularly highlight the interface between antimony-filled regions and residual pores, confirming the absence of reaction phases at the carbon-antimony boundary.

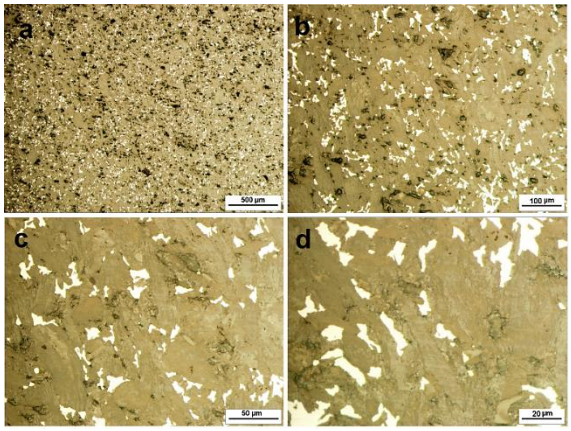

Fig. 13. Optical micrographs of graphite/antimony composite at (a) 50×, (b) 200×, (c) 500× and (d) 1000× magnification.

4. Conclusion

1.SPS achieved 3 cm antimony impregnation depth in 9 minutes, applicable to other metals.
2.X-ray imaging provided clear insights into infiltration geometry/depth.
3.Temperature/displacement data enabled process optimization.
4.Mechanical pressure (10 MPa) and vacuum synergistically enhanced speed/depth.
5.Property improvements (density, porosity, strength) confirmed effective pore filling by antimony.

Acknowledgement

This research work has been supported with a research grant (No.: 380682) by the Materials and Energy Research Centre (MERC), Karaj, Iran.

References

[1] Huebner M, Young LA. Materials for mechanical seals. Encyclopedia of Tribology. 2013;2173-2184.
[2] Ramanathan A, Krishnan PK, Muraliraja R. A review on the production of metal matrix composites through stir casting–Furnace design, properties, challenges, and research opportunities. J. Manu, Proc. 2019 ;1,42:213-245.
[3] Rumble JR, ed. CRC Handbook of Chemistry and Physics. 104th ed. Boca Raton: CRC Press; 2023.
[4] Chen Y, Dong L, Liu C, Xu J, Yang Z. Study on performance change of phenolic resin impregnated graphite in acid environment. In IOP Conference Series: Earth and Environmental Science 2021; Mar 1 Vol. 692, No. 3:p. 032077. IOP Publishing.
[5] Stec J, Tarasiuk J, Wroński S, Kubica P, Tomala J, Filipek R. Investigation of molten metal infiltration into micropore carbon refractory materials using X-ray computed tomography. Materials. 2021; 8,14:3148-3155.
[6] Ma S, Xu E, Zhu Z, Liu Q, Yu S, Liu J, Zhong H, Jiang Y. Mechanical and wear performances of aluminum/sintered-carbon composites produced by pressure infiltration for pantograph sliders. Powder Technology. 2018 ; 15,326:54-61.
[7] Li Y, Huang J, Wang M, Liu J, Wang C, Zhong H, Jiang Y. Microstructure and current carrying wear behaviors of copper/sintered–carbon composites for pantograph sliders. Metals and Materials International. 2021 ;27:3398-3408.
[8] Pierson HO. Handbook of carbon, graphite, diamond and fullerenes, Noyes publications. Mill Road, Park Ridge, NJ. 1993;43.
[9] Quenisset JM. Carbon combinations. Carbon—Carbon composites. By Savage G, Chapman & Hall, London 1993; 389
[10] Wang Q, He M, Li X, Hao L. Preparation and properties of graphite/antimony composites based on coal tar pitch. Advanced Composites Letters. 2017 ;Mar;26(2):096369351702600204.
[11] Rahimipour MR, Majidian H, Zakeri M, Razavi M, Shirani M. Investigation of the rheology of coal tar bitumen under different temperature, time and atmospheric conditions. Mater Energy Res Cent. 2017.
[12] Yang ZZ, Zhang CY, Ou YQ, Su ZK, Zhao Y, Cong HJ, Ai XP, Qian JF, Amorphous Sb/C composite with isotropic expansion property as an ultra-stable and high-rate anode for lithium-ion batteries, Rare Metal. 2024;43:2039-2052.
[13] Meunier V, Ania C , Bianco A, Chen Y, Choi GB, Kim Y,Koratkar N,Liu C, Tascon M. Carbon science perspective in 2022: Current research and future challenges, Carbon. ;2022,195:272-291.